Power Electronic Systems
Laboratory

Proceedings of the IEEE International Electric Machines & Drives Conference (IEMDC 2021),
Connecticut, USA, May 17-21, 2021

Design and Experimental Analysis of a Selfbearing Double-Stator Linear-Rotary Actuator

S. Miric,
R. Giuffrida,
G. Rohner,
D. Bortis,
J. W. Kolar

Eidgenössische Technische Hochschule Zürich
Swiss Federal Institute of Technology Zurich

Design and Experimental Analysis of a Selfbearing Double-Stator Linear-Rotary Actuator

Spasoje Mirić, Rosario Giuffrida, Gwendolin Rohner, Dominik Bortis and Johann W. Kolar
Power Electronic Systems Laboratory (PES)
ETH Zurich, Switzerland, miric@lem.ee.ethz.ch

***Abstract*—Linear-rotary actuators (LiRAs) are today used in industry applications where a controlled linear and rotary motion is necessary such as pick-and-place robots, servo actuation of gearboxes or tooling machines. However, in special industry applications that require high purity and/or high precision positioning, the usage of conventional LiRAs with mechanical bearings is limited. Therefore, in this paper a LiRA with integrated magnetic bearings, i.e. a selfbearing/bearingless LiRA, is analyzed. The actuator employs concentrically arranged linear and rotary stators placed inside and outside a cylindrically shaped mover, which results in a so-called selfbearing double-stator (SBDS) LiRA. A FEM geometry optimization of the SBDS LiRA is performed and Pareto performance plots concerning linear force and torque generation are obtained. A SBDS LiRA hardware demonstrator and an 18-phase inverter power supply hardware prototype are built and their operation is experimentally verified by rotary and linear position step response measurements.**

***Index Terms*—GaN Inverter, Linear-Rotary Actuators, Machine Geometry Pareto Optimization, Magnetic Bearings, Selfbearing, Bearingless**

I. Introduction

In systems that simultaneously require controlled linear and rotary motion, direct drive linear-rotary actuators (LiRAs) are typically used. Examples of such systems are servo actuation of gearboxes [1], pick-and-place robots in semiconductor industry [2] and robot joints [3], to mention a few. LiRAs may be realized by coupling linear and rotary actuators in different ways, e.g. the rotary actuator can move the whole linear actuator or the linear and the rotary actuators can share the same mover [4]. An overview of possible LiRA coupling options can be found in [5]. Also, it is possible to have the stators displaced radially and/or arranged concentrically, resulting in a double-stator (DS) LiRA as shown in [6]. In this paper such type of the actuator, i.e. a DS LiRA, is analyzed. Compared to a conventional LiRA system, the analyzed DS LiRA has integrated magnetic bearings (MBs), as shown in **Fig. 1**. MBs offer several advantages such as possible usage in high purity applications and longer lifetime as no mechanical wear occurs or mover tilting control, advantageous in high precision pick-and-place applications [7]. Particularly, in food or pharmaceutical industries, actuators require high-purity and regular high-pressure washdowns, for what typically mechanical bearings have to be disassembled, resulting in larger downtimes and cost [8]. Advantageously, washdowns of SBDS LiRAs could be directly performed, without a need to disassemble any part, since an air gap between the mover and the stator is maintained with magnetic bearing forces.

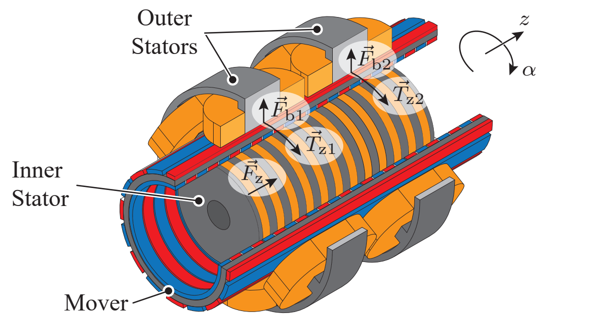

Fig. 1: SBDS LiRA with the outer rotary stators for the torque and the bearing force generation and the inner stator for the linear (axial) force generation.

In the following sections the proposed selfbearing DS (SBDS) LiRA design and optimization (cf. **Sec. II**), hardware prototype manufacturing (cf. **Sec. III**), inverter power supply design and manufacturing (cf. **Sec. IV**) and measurement results of the experimental analysis of a hardware demonstrator (cf. **Sec. V**) are presented.

II. Actuator Topology and Geometry Optimization

A. SBDS LiRA Geometry Parameters

The analyzed SBDS LiRA is shown in **Fig. 1**, where the outer rotary stators generate the torques $\vec{T}_{z1}$ and $\vec{T}_{z2}$ and the bearing forces $\vec{F}_{b1}$ and $\vec{F}_{b2}$, while the inner linear stator generates the linear (axial) force $\vec{F}_z$ on the mover. Typically, the total generated torque on the mover $\vec{T}_z$ is equally divided between the rotary stators, i.e. $\vec{T}_{z1} = \vec{T}_{z2} = \vec{T}_z/2$, where the bearing forces $\vec{F}_{b1}$ and $\vec{F}_{b2}$ may be different and depend on the desired tilting of the mover and the radial load on the mover.

To determine an optimal SBDS LiRA geometry, an optimization based on a grid search method is performed. The method evaluates all possible designs for a given discrete design space of the parameters and it does not need any cost function. As both, magnetic and thermal performance of the SBDS LiRA depend on its geometry, it is necessary to establish magnetic (2D FEM) and thermal (analytic) models and evaluate them for each discrete point of the design space. The considered SBDS LiRA geometry parameters are shown in **Fig. 2**. Some of the parameters are kept fixed and some are swept in the optimization. The fixed parameters are given

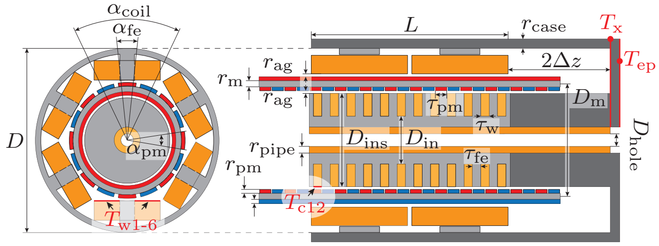

Fig. 2: SBDS LiRA parametrized geometry used in the optimization.

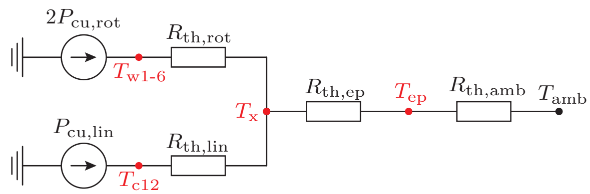

Fig. 3: Lumped parameter steady-state thermal model. Important temperature measurement points (T_{w1-6}, T_{c12}, T_x, T_{eq}) are denoted in **Fig. 2** in the SBDS LiRA geometry.

TABLE I: Fixed geometry parameters.

Symbol	Description	Value
Geometrical		
L	Active length	$100\,\mathrm{mm}$
D	Outer diameter	$100\,\mathrm{mm}$
Δz	Axial stroke	$30\,\mathrm{mm}$
r_{ag}	Magnetic air gap	$0.7\,\mathrm{mm}$
D_{hole}	Cu pipe inner diam.	$8\,\mathrm{mm}$
Magnetic/Electric		
B_r	PM magnetization	$1.3\,\mathrm{T}$
$\mu_{r,fe}$	Iron core rel. perm.	400
k_{ff}	Wind. fill factor	0.6
$N_{p,rot}$	Num. of rot. poles	16
$N_{p,lin}$	Num. of lin. poles	16
$N_{s,rot}$	Num. of rot. slots	6
$N_{s,lin}$	Num. of lin. slots	12
Thermal		
T_{amb}	Ambient temperature	$35\,^{\circ}\mathrm{C}$
$T_{w,max}$	Max. winding hot spot temp.	$140\,^{\circ}\mathrm{C}$
λ_w	Therm. cond. of wind.	$2\,\mathrm{W/(mK)}$
λ_{cu}	Therm. cond. of copper	$385\,\mathrm{W/(mK)}$
λ_{fe}	Therm. cond. of iron	$20\,\mathrm{W/(mK)}$
λ_{alu}	Therm. cond. of alum.	$200\,\mathrm{W/(mK)}$
λ_{ex}	Therm. cond. of epoxy	$0.1\,\mathrm{W/(mK)}$

in **Tab. I**, where the swept parameters are listed in **Tab. II**. Some of the swept parameters are dependent by an expression to other geometrical parameters, as denoted in the last column in **Tab. II**.

B. Geometry Optimization

Prior to performing a geometry optimization it is necessary to establish magnetic and thermal models. The magnetic model is a magnetostatic 2D FEM model, which is formed by coupling MATLAB and ANSYS, i.e. a MATLAB script is written that creates a 2D FEM model in ANSYS, performs magnetostatic simulations, saves results and closes the ANSYS program. The thermal model is a lumped parameter steady-state model that consists of copper loss sources and

TABLE II: Swept geometry parameters.

Symbol	Range	Step	Expression
$k_{in,out}$	$[0.78,\ldots,0.9]$	0.02	D_m/D
$k_{cu-fe,rot}$	$[0.78,\ldots,0.9]$	0.02	$1-\alpha_{fe}/\alpha_{coil}$
$k_{cu-fe,lin}$	$[0.5,\ldots,0.7]$	0.01	$\tau_w/(\tau_w-\tau_{fe})$
$k_{pm,rot}$	$[0.7,\ldots,0.9]$	0.1	$\alpha_{pi}/(2\pi/N_{p,rot})$
$k_{pm,lin}$	$[0.8,0.9]$	0.1	$\tau_{pm}/(L/N_{p,lin})$
r_m	$[2.5,\ldots,4]\mathrm{mm}$	$0.5\,\mathrm{mm}$	-
r_{pm}	$[2,2.5]\mathrm{mm}$	$0.5\,\mathrm{mm}$	-
r_{pipe}	$[2,\ldots,3]\mathrm{mm}$	$0.5\,\mathrm{mm}$	-

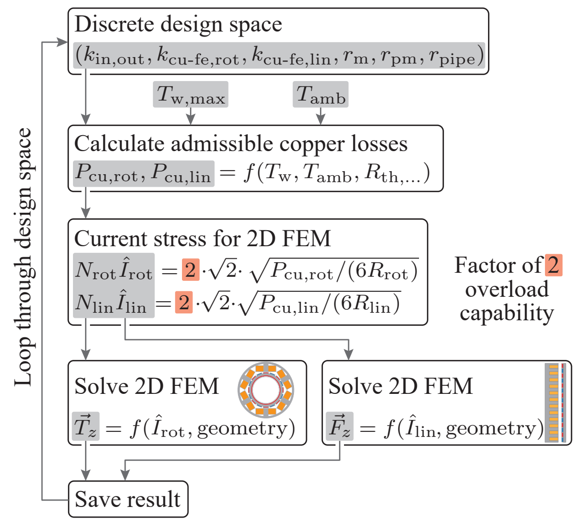

Fig. 4: Geometry optimization algorithm where first the admissible copper losses are calculated based on the established thermal model (cf. **Fig. 3**). From the admissible copper losses current stresses are obtained, which are used for the magnetic 2D FEM models where the torque $\vec{T}_z$ and the linear force $\vec{F}_z$ are calculated. This sequence of calculations is repeated for all geometry options defined by the discrete design space. The electrical resistance of a single rotary/linear coil is denoted as R_{rot}/R_{lin}. The considered current stress is twice as high than allowed by the stationary thermal properties of the SBDS LiRA, such that a chosen design finally features a factor of 2 of overload capability, without saturation of the magnetic parts occurring.

thermal resistances calculated based on the assumed thermal conductivities given in **Tab. I**. The detailed calculation of each thermal model element is omitted here as it is a basic task once the thermal conductivities are assumed. Accordingly, only an equivalent thermal model is given in **Fig. 3**, where at the temperature measurement point T_x (cf. **Fig. 2**) the heat flows from the outer rotary stator and the inner stator merge. The thermal resistances $R_{th,rot}$ and $R_{th,lin}$ are the total thermal resistances between the winding hot spot temperatures (T_{w1-6} for the rotary stator and T_{c12} for the linear stator, cf. **Fig. 2**) and T_x, i.e. the region where both stators are mechanically attached. Further, $R_{th,ep}$ represents a thermal resistance of the aluminum end plate, which is proportional to the end plate thickness r_{case}. Finally, a thermal resistance between the SBDS LiRA end plate and the ambient is estimated assuming a pin fin heatsink with a diameter of $98\,\mathrm{mm}$, a height of $50\,\mathrm{mm}$ and forced convection with $2\,\mathrm{m/s}$ air speed, which results in

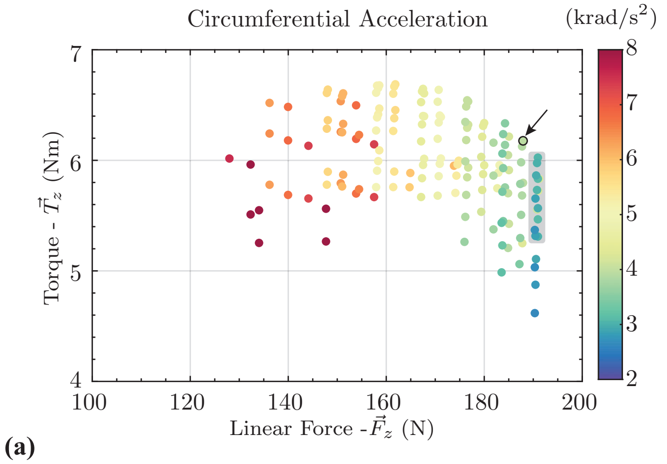

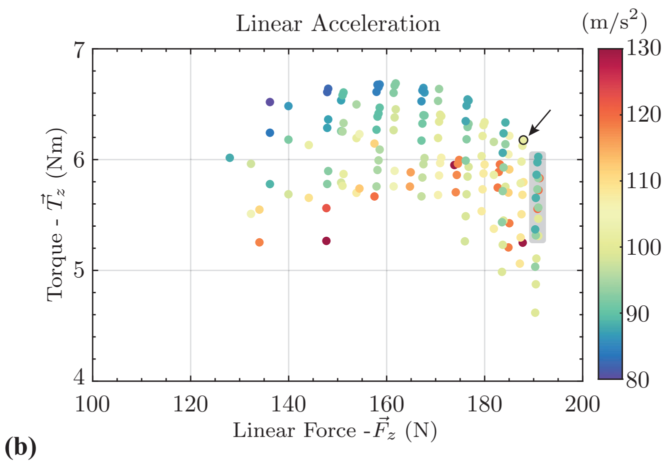

Fig. 5: Pareto performance plots obtained using the optimization algorithm shown in **Fig. 4**. Torque $\vec{T}_z$ versus linear force $\vec{F}_z$ where by color **(a)** circumferential and **(b)** linear (axial) accelerations are given. The expected trade-off between torque and linear force can be seen, since e.g. increasing the size of the inner stator reduces the outer stator size, and vice versa. This design trade-off can also be shown by scaling laws for the outer rotary and inner linear actuators, cf. [5]. The chosen design has the following continuous operation performance: torque - 6.24 Nm, linear force - 181.5 N, circumferential acceleration - 5.3 krad/s^2 and linear acceleration - 123.5 m/s^2.

a thermal resistance of $R_{\mathrm{th,amb}} = 0.5\,\mathrm{K/W}$, cf. [9].

The allowed copper losses per rotary stator, $P_{\mathrm{cu,rot}}$, and in the linear stator, $P_{\mathrm{cu,lin}}$, can be calculated from the obtained thermal resistances and the assumed winding hot spot ($T_{\mathrm{w1-6}} = T_{\mathrm{c12}} = T_{\mathrm{w,max}}$) and ambient temperatures T_{amb}, where $T_{\mathrm{w,max}}$ and T_{amb} are given in **Tab. I**. By solving the circuit in **Fig. 3**, copper losses are calculated as

$$
\begin{aligned}
P_{\mathrm{cu,rot}} &= \frac{R_{\mathrm{th,lin}}}{2R_{\mathrm{th,par}}(R_{\mathrm{th,rot}} + R_{\mathrm{th,lin}})}(T_{\mathrm{w,max}} - T_{\mathrm{amb}}),\\
P_{\mathrm{cu,lin}} &= \frac{R_{\mathrm{th,lin}}}{R_{\mathrm{th,par}}(R_{\mathrm{th,rot}} + R_{\mathrm{th,lin}})}(T_{\mathrm{w,max}} - T_{\mathrm{amb}}),
\end{aligned}
\tag{1}
$$

where

$$
R_{\mathrm{th,par}} = \frac{R_{\mathrm{th,rot}}R_{\mathrm{th,lin}}}{R_{\mathrm{th,rot}} + R_{\mathrm{th,lin}}} + R_{\mathrm{th,ep}} + R_{\mathrm{th,amb}}. \tag{2}
$$

TABLE III: Chosen Design Parameters.

Symbol	Description	Value
$k_{\mathrm{in,out}}$	Ratio of outer and mover diameter	0.56
$k_{\mathrm{cu-fe,rot}}$	Ratio of copper and iron core material	0.8
$k_{\mathrm{cu-fe,lin}}$	Ratio of copper and iron core material	0.5
$k_{\mathrm{pm,rot}}$	Relative amount of PM withing a pole	0.8
$k_{\mathrm{pm,lin}}$	Relative amount of PM withing a pole	0.9
r_{m}	Mover thickness	3 mm
r_{pm}	PM thickness	2 mm
r_{pipe}	Copper pipe wall thickness	2.5 mm

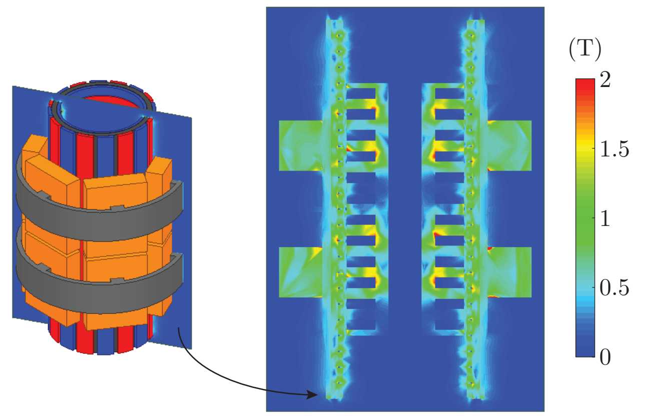

Fig. 6: 3D FEM flux density distribution of the chosen design, cf. **Fig. 5**. The simulation is done for twice the thermally allowed current ($N_{\mathrm{rot}}\hat{I}_{\mathrm{rot}} = 2028.6$ Aturns and $N_{\mathrm{lin}}\hat{I}_{\mathrm{lin}} = 685.2$ Aturns), in order to check for eventual saturation of the SBDS LiRA iron parts.

After the thermally permissible electrical loading of the SBDS LiRA windings is determined, the allowed ampere turns for the rotary and linear stators are calculated, as shown in the optimization algorithm in **Fig. 4**. From the ampere turns, the current density in the SBDS LiRA rotary and linear stators is obtained and it is used for 2D FEM magnetic simulations where the torque $\vec{T}_z$ and the linear force $\vec{F}_z$ are calculated, cf. **Fig. 4**. In post processing, all the necessary data, such as mass, volume of the parts and circumferential and linear accelerations, are calculated.

C. Optimization Results

The optimization results are shown in **Fig. 5**, where torque versus linear force is plotted and the related accelerations are given by the color of the dots. The total number of design combinations in the discrete design space is 24192, but in **Fig. 5** only the performance of 158 parameter combinations is shown. These are the only valid designs where the saturation of the iron core parts does not occur. More specifically, the flux density level in any point of the SBDS LiRA magnetic parts satisfies the following: $< 2.1\,\mathrm{T}$ for the outer stator (electrical steel), $< 1.4\,\mathrm{T}$ for the inner stator (steel ST52) and $< 2.1\,\mathrm{T}$ for the mover back iron (soft iron). Additionally, it should be mentioned that the shown designs feature a factor of 2 of overload capability, i.e. for a short time the SBDS LiRA may generate twice the torque/force that is thermally possible in continuous operation. The chosen design in **Fig. 5** does not feature the maximum possible linear force as according

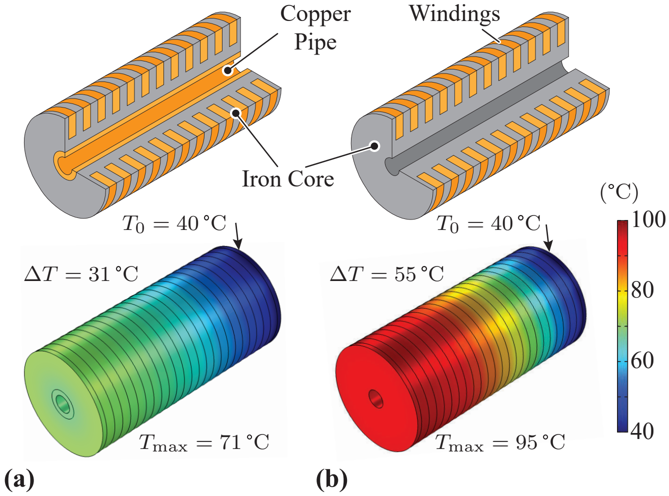

Fig. 7: Temperature distribution in the inner linear stator due to axial heat flow **(a)** with and **(b)** without an inserted copper pipe for enhancing heat conduction. The temperature distribution is obtained with FEM simulations, where the loss density in the copper windings is assumed to be $p_{\mathrm{cu}} = \rho_{\mathrm{cu}}\hat{J}^2/2 = 4.1 \times 10^5\ \mathrm{W/m^3}$, which is obtained by assuming $\rho_{\mathrm{cu}} = 2.27 \times 10^{-8}\ \Omega\mathrm{m}$ at $110\,°\mathrm{C}$ and a typical current density peak value of $\hat{J} = 6\ \mathrm{A/mm^2}$. The assumed thermal conductivities are: $20\ \mathrm{W/(mK)}$ for the iron core, $2\ \mathrm{W/(mK)}$ for the windings (cf. [11]) and $385\ \mathrm{W/(mK)}$ for the copper pipe. The assumed winding fill factor is 0.6. Geometric dimensions correspond to **Tabs. I** and **III**.

designs have significantly lower accelerations (shaded in gray) due to a larger mass/moment of inertia, cf. [10]. Therefore, a design with slightly lower axial force is chosen, as denoted with an arrow. The geometrical parameters of the chosen design are given in **Tab. III**. Finally, a 3D FEM model of the SBDS LiRA is established and the chosen design is verified; e.g. the resulting flux density distribution is shown in **Fig. 6**. The current density is twice the thermally allowed stationary value, but there is no saturation of the iron parts.

D. Effect of the Copper Pipe on Cooling

To show the effect of the copper pipe on the cooling of the inner linear stator of the SBDS LiRA, the chosen design is simulated. The inner stator of the SBDS LiRA is held from one axial end with a mechanical assembly, which is also used for cooling, i.e. an axial conductive heat flow through the inner stator is assumed. A consequence of the axial heat flow is a temperature difference along the inner stator, which can be rather high. In order to reduce this temperature difference and also the total axial thermal resistance, a design with a copper pipe inserted inside the inner stator back iron is proposed, as shown in **Fig. 7(a)**. Due to around 20 times higher thermal conductivity of the copper compared to the stator iron core the total axial thermal resistance reduces, but the reduction of cross section of the magnetic iron core material potentially causes magnetic saturation of the inner stator and limits its overload capability. Therefore, there is an optimum amount of 'magnetically' and 'thermally' conductive materials in the inner linear stator that leads to a maximum linear force per unit of copper loss, which is determined in the established optimization routine. The effect of the copper pipe on the cooling of the inner stator is clearly shown in **Fig. 7**, where the optimized design geometry is simulated with and without a copper pipe.

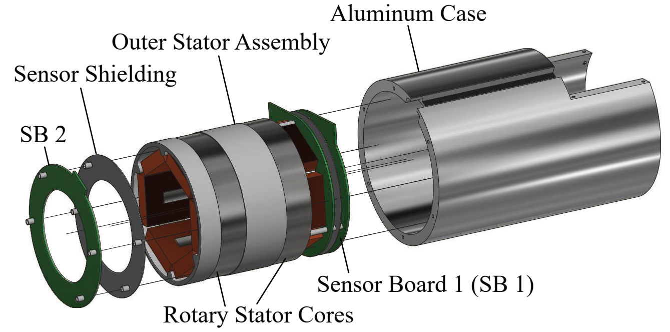

Fig. 8: CAD model of the SBDS LiRA outer rotary stator prototype, with PCB position sensor boards at both axial ends and a power connection PCB. The rotary stator core and windings are inserted into an aluminum case and potted.

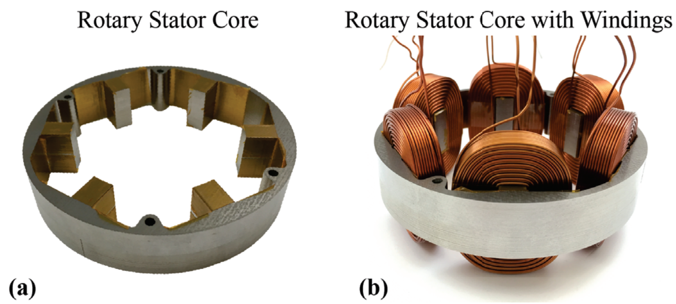

Fig. 9: Hardware realization of the SBDS LiRA stator parts: **(a)** Outer stator rotary core with $0.35\ \mathrm{mm}$ thick laminated sheets and Kapton tape insulation. **(b)** Rotary stator windings realized with $0.8\ \mathrm{mm}$ wire diameter and 190 turns.

III. SBDS LiRA Hardware Realization

After the SBDS LiRA geometry is optimized and all geometrical parameters are determined, a CAD model of the prototype is established. In **Fig. 8** the model of the outer rotary stator is shown. In order to magnetically levitate the mover of the SBDS LiRA, position sensors are needed on both axial ends of the actuator, which are realized on a PCB. Therefore, two sensor PCBs, SB1 and SB2, are assumed. For the winding power connections, also a PCB is used as there are $2\,\mathrm{stators} \times 6\,\mathrm{coils} \times 2\,\mathrm{wire\ ends} = 24$ wire connections.

The chosen SBDS LiRA design (see Pareto plot in **Fig. 5**) is realized in hardware. In **Fig. 9** the outer rotary stator core without and with the concentrated windings is shown. The stator core is realized from electrical steel laminations and it is insulated from the windings with Kapton tape. The windings are built from a self-bonding wire such that no coil former is needed, where the wire diameter and the number of turns (N_{rot}) are determined from the following considerations. The upper limit on the wire diameter is obtained by considering skin effect and/or the skin depth $\delta_{\mathrm{cu,rot}} =$

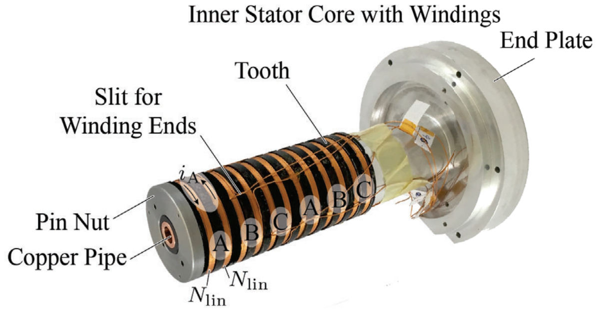

Fig. 10: Inner linear stator of the SBDS LiRA with inserted copper pipe for enhanced cooling. The windings are realized with $0.5\,\mathrm{mm}$ wire diameter and $2 \times N_{\mathrm{lin}}$ turns, where $N_{\mathrm{lin}} = 150$.

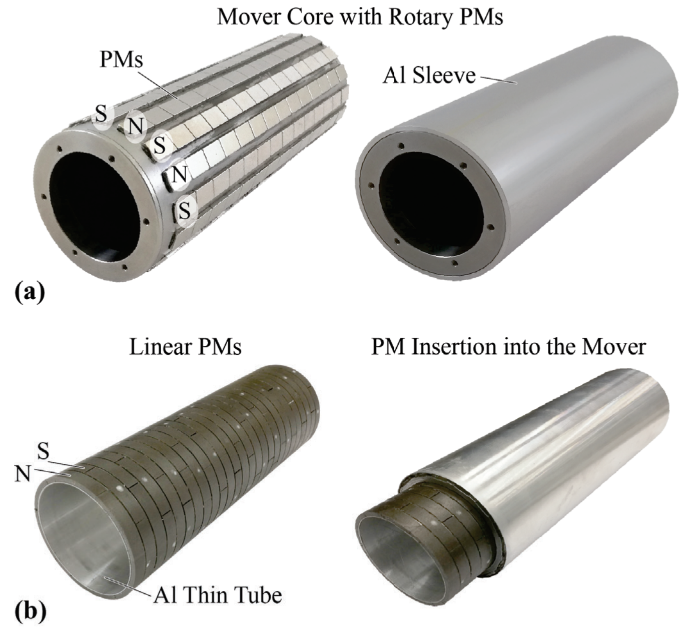

Fig. 11: SBDS LiRA mover hardware prototype: **(a)** Mover iron core with the outer rotary PM poles alternated in circumferential direction. The outer rotary PMs are covered with a $0.4\,\mathrm{mm}$ thick aluminum sleeve for mechanical protection and an eddy current based radial position sensing. **(b)** Inner linear PM poles alternated in axial direction, where the PMs are glued onto the aluminum cylindrical form. The linear stator PMs are finally inserted into the mover back iron.

$\sqrt{2\rho_{\mathrm{cu}}/(\mu_0 \cdot \omega)} = 3.26\,\mathrm{mm}$, where $\rho_{\mathrm{cu}} = 1.68 \times 10^{-8}\,\Omega\mathrm{m}$, $\mu_0 = 4\pi \times 10^{-7}\,\mathrm{H/m}$ and the angular frequency is calculated assuming a maximum rotor speed of $\omega = \omega_{\mathrm{rot}} = N_{\mathrm{p,rot}} \cdot (\pi/30) \cdot 3000\,\mathrm{rpm} = 2513.3\,\mathrm{rad/s}$; $N_{\mathrm{p,rot}} = 16$ is the number of PM poles of the mover on the outer rotary side, cf. **Tab. I**. Typically, in electric machine design, the maximum wire diameter is set such that it is smaller than either a half ($< \delta_{\mathrm{cu,rot}}/2$) or a quarter ($< \delta_{\mathrm{cu,rot}}/4$) of the expected skin depth $\delta_{\mathrm{cu,rot}}$. Since the SBDS LiRA stator has open tooth and the windings are exposed to the PM field, the wire diameter is chosen considering $D_{\mathrm{wire,rot}} < \delta_{\mathrm{cu,rot}}/4 = 0.81\,\mathrm{mm}$, resulting in $D_{\mathrm{wire,rot}} = 0.8\,\mathrm{mm}$. The number of turns N_{rot} is estimated from the available winding window area $A_{\mathrm{w,rot}} = 148.7\,\mathrm{mm}^2$ as $N_{\mathrm{rot}} = \mathrm{round}(k_{\mathrm{ff}} \cdot A_{\mathrm{w,rot}}/A_{\mathrm{wire,rot}}) = 187\,\mathrm{turns}$, where $k_{\mathrm{ff}} = 0.6$ is the fill factor and $A_{\mathrm{wire,rot}} = \pi D^2_{\mathrm{wire,rot}}/4 = 0.5\,\mathrm{mm}^2$ is the wire cross section area. Finally, the prototype is built with $N_{\mathrm{rot}} = 190\,\mathrm{turns}$, cf. **Fig. 9**. The maximum expected induced voltage in the rotary coil is estimated using the total flux in the tooth $\hat{\Phi}_{\mathrm{rot}} = 0.11\,\mathrm{mWb}$ (calculated using 3D FEM simulation), as $\hat{E}_{\mathrm{rot}} = N_{\mathrm{rot}} \cdot \omega_{\mathrm{rot}} \cdot \hat{\Phi}_{\mathrm{rot}} = 52.5\,\mathrm{V}$. From the thermally allowed ampere turns, the phase current peak value is $\hat{I}_{\mathrm{rot}} = 1014\,\mathrm{Aturns}/N_{\mathrm{rot}} = 5.3\,\mathrm{A}$. The values for the induced voltage and the phase current, $\hat{E}_{\mathrm{rot}}$ and $\hat{I}_{\mathrm{rot}}$, are used later for the inverter design.

A similar winding design approach is applied for the inner linear stator of the SBDS LiRA. The maximum electrical frequency is calculated as $\omega_{\mathrm{lin}} = (2\pi/\tau_{\mathrm{pp}})v_{\mathrm{z}} = 502.6\,\mathrm{rad/s}$, where $\tau_{\mathrm{pp}} = 2L/N_{\mathrm{p,lin}} = 12.5\,\mathrm{mm}$ is the linear actuator pole pair size and $v_{\mathrm{z}} = 1\,\mathrm{m/s}$ is the assumed maximum linear speed. For this angular frequency, the skin depth is $\delta_{\mathrm{cu,lin}} = 7.3\,\mathrm{mm}$, which imposes the limit on the maximum wire diameter $D_{\mathrm{wire,lin}} < \delta_{\mathrm{cu,lin}}/4 = 1.82\,\mathrm{mm}$. As a wire of such large diameter would be difficult to wind onto the stator core, the wire diameter is estimated such that a similar induced voltage is obtained as for the rotary winding, which allows to supply both windings (rotary and linear) from the same DC link inverter. Therefore, in the first step the number of winding turns is obtained as $N_{\mathrm{lin}} = \mathrm{round}(\hat{E}_{\mathrm{lin}}/(\omega_{\mathrm{lin}} \cdot \hat{\Psi}_{\mathrm{lin}})) = 156\,\mathrm{turns}$, where $\hat{E}_{\mathrm{lin}} = \hat{E}_{\mathrm{rot}} = 52.5\,\mathrm{V}$ and $\hat{\Psi}_{\mathrm{lin}} = 0.672\,\mathrm{mWb}$ (obtained from 3D FEM simulation). The wire cross section area is calculated as $A_{\mathrm{wire,lin}} = k_{\mathrm{ff}} \cdot A_{\mathrm{w,lin}}/N_{\mathrm{lin}} = 0.18\,\mathrm{mm}^2$, which results in a wire diameter of $D_{\mathrm{wire,lin}} = 2\sqrt{A_{\mathrm{wire,lin}}/\pi} = 0.48\,\mathrm{mm}$, which also satisfies the skin depth condition. Finally, the inner linear stator winding is realized with a wire diameter of $D_{\mathrm{wire,lin}} = 0.5\,\mathrm{mm}$, cf. **Fig. 10**. The prototype employs $N_{\mathrm{lin}} = 150\,\mathrm{turns}$ per coil, where two coils constitute a phase winding, e.g. two coils around a tooth are carrying the same phase current but in opposite directions, as denoted for phase A in **Fig. 10**. For the prototype realization of the inner linear stator (cf. **Fig. 10**), the stator iron core is used as 'coil former' where individual coils are wound on the stator core pieces and afterwards all coils are pressed with a pin nut to form the overall stator. The copper pipe is press fitted into the stator iron core, such that a good thermal contact is established.

The mover hardware prototype realization is shown in **Fig. 11**. The rotary set of PMs is glued on the outer side of the mover back iron and covered with an aluminum sleeve, cf. **Fig. 11(a)**. Mounting of the inner set of PMs was performed in two steps: first the PMs are glued onto a thin aluminum tube which is then inserted into the cylindrical mover, cf. **Fig. 11(b)**. The assembled mover shows a mass of $m = 1.24\,\mathrm{kg}$ and a moment of inertia of $J = 0.001\,45\,\mathrm{kgm}^2$.

Before assembly, the rotary stator core with windings is inserted into an aluminum case (cf. **Fig. 8**) and potted with epoxy: WEVOPOX 2513 mixed with WEVODUR HC1003 in ratio $100 : 13$. In the next step, the outer and the inner stators (cf. **Fig. 9** and **Fig. 10**) are mechanically assembled as shown

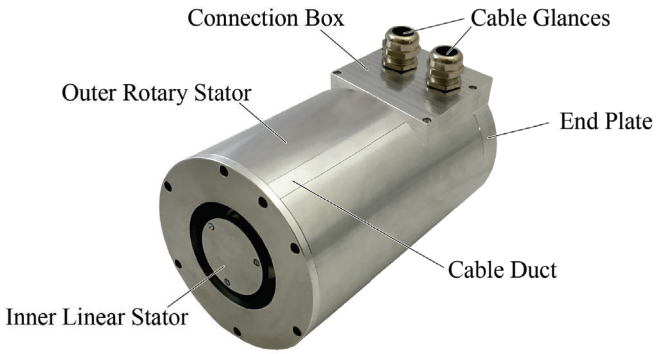

Fig. 12: SBDS LiRA prototype with the outer rotary (cf. **Fig. 8** and **Fig. 9**) and the inner linear (cf. **Fig. 10**) stators assembled.

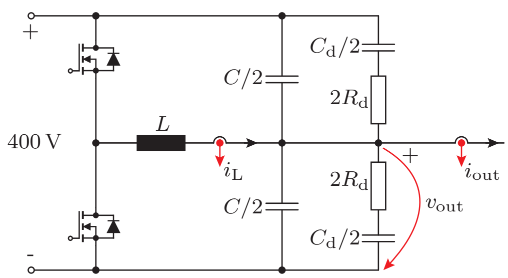

Fig. 13: SBDS LiRA circuit schematic of an inverter phase with output filter inductor $L = 80\,\mu\mathrm{H}$ and filter capacitor $C = 4.8\,\mu\mathrm{F}$. The damping resistance $R_{\mathrm{d}} = 6\,\Omega$ and capacitance $C_{\mathrm{d}} = C$ are chosen according to [14], considering $n = 1$.

in **Fig. 12**. The connection box has two cable glances, one for the power cable [12] and another one for the sensor cable [13]. The cable duct is used to connect the PCB integrated position sensors SB 2 with the inverter control, cf. **Fig. 8**.

IV. 18-Phase Inverter Hardware Realization

In order to supply the SBDS LiRA, an inverter stage is designed and realized in hardware. In **Fig. 13** a schematic of a single inverter phase with an LC output filter is shown. On one hand, the output filter reduces high frequency noise in the output current and provides a 'smooth' output voltage to the SBDS LiRA stator windings, which also increases the signal-to-noise ratio of integrated position sensors which is important for precise position control and high control bandwidth of the actuator (cf. [15]). On the other hand, the output filter due to its low pass nature limits the output voltage v_{out} and consequently the output current i_{out} control dynamics. Additionally, it complicates the current controller design as three cascaded control loops have to be implemented: (1) inner i_{L} current control loop; (2) middle v_{out} output (capacitor) voltage control loop and (3) outer i_{out} output current control loop.

Based on the voltage and current requirements of the SBDS LiRA, the specifications for the inverter design and optimization are defined and given in **Tab. IV**. The switching frequency is selected as $f_{\mathrm{sw}} = 140\,\mathrm{kHz}$ as typical for $400\,\mathrm{V}$ GaN inverter systems. A total of 15 phases of the SBDS LiRA are to be supplied. As the inverter features $18\,\mathrm{phases}$ it could also be used to supply other types of actuators such as magnetically levitated tubular linear actuators with $18\,\mathrm{phases}$ [16].

TABLE IV: SBDS LiRA Inverter Specifications.

Symbol	Description	Value
V_{dc}	DC link voltage	$400\,\mathrm{V}$
$\hat{I}_{\mathrm{out}}$	Output phase current peak	$10\,\mathrm{A}$
f_{out}	Output fundamental frequency	$400\,\mathrm{Hz}$
f_{sw}	Switching frequency	$140\,\mathrm{kHz}$
N_{ph}	Number of phases	18

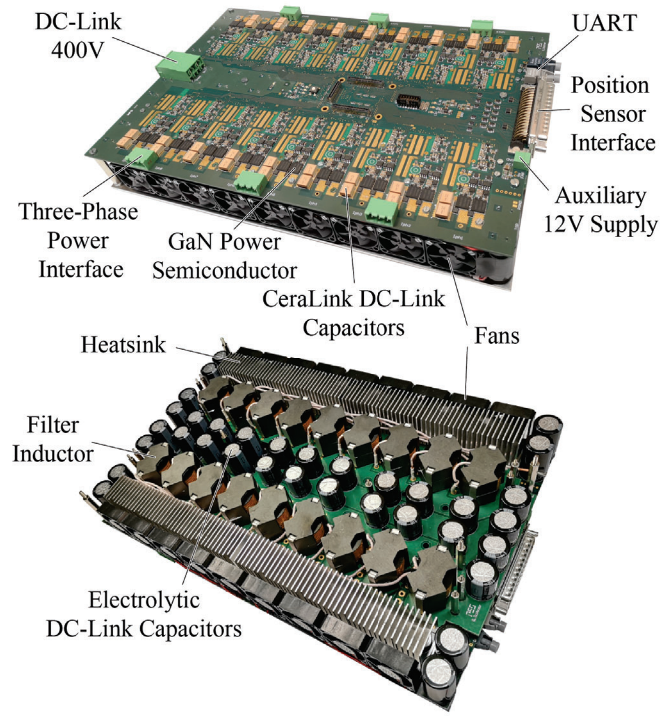

Fig. 14: Top and bottom view of the SBDS LiRA inverter prototype. The inverter has a single power input supplied from a $400\,\mathrm{V}$ DC source and features 6×3 phase outputs. The inverter features a UART communication interface and a position sensor interface. The low voltage circuitry is supplied from a $12\,\mathrm{V}$ auxiliary supply.

The inverter hardware prototype is shown in **Fig. 14**, whose heatsink and output filter inductor have been optimized for efficiency and power density. The used power semiconductors are $600\,\mathrm{V}$, $70\,\mathrm{m}\Omega$ CoolGaN-MOSFETs [17]. The inductor is realized with ferrite N87 RM12 core, which has $80\,\mu\mathrm{H}$ inductance achieved with $23\,\mathrm{turns}$ of $1.8\,\mathrm{mm}$ diameter litz wire ($300 \times 71\,\mu\mathrm{m}$ strands).

V. Experimental Analysis

The SBDS LiRA (cf. **Fig. 12**) is mounted into a customized test-bench where the mover can be held via auxiliary mechanical bearings until the magnetic bearings are commissioned. The test-bench features a torque sensor (cf. [18]), force sensors for the bearing force measurements (cf. [19]) and a force sensor for the linear force measurement (cf. [20]).

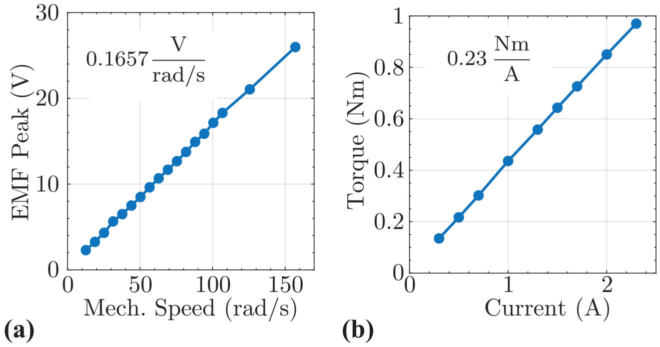

Fig. 15: **(a)** Voltage constant $K_{\mathrm{V,rot}}$ measurement of the rotary stator where the SBDS LiRA mover is rotated and the peak value of the induced back EMF per phase is measured. From the measurement results a voltage constant of $K_{\mathrm{V,rot}} = 0.1657\,\mathrm{V/(rad/s)}$ is deduced. **(b)** Torque constant K_{T} measurement where the SBDS LiRA mover is fixed and the torque is measured with a torque sensor (cf. [18]) while changing the current amplitude. From the measurement results a torque constant of $K_{\mathrm{T}} = 0.23\,\mathrm{Nm/A}$ is deduced.

TABLE V: SBDS LiRA Simulated and Measured Parameters.

Symbol	Unit	Value Sim.	Value Meas.	Error (%)
Rotary Stator				
$\hat{\Psi}_{\mathrm{rot}}$	mWb	20.9	20.71	0.91
K_{T}	Nm/A	0.25	0.23	8.7
Linear Stator				
$\hat{\Psi}_{\mathrm{lin}}$	mWb	100.8	110.8	9.0
K_{L}	N/A	83.53	76.01	9.0

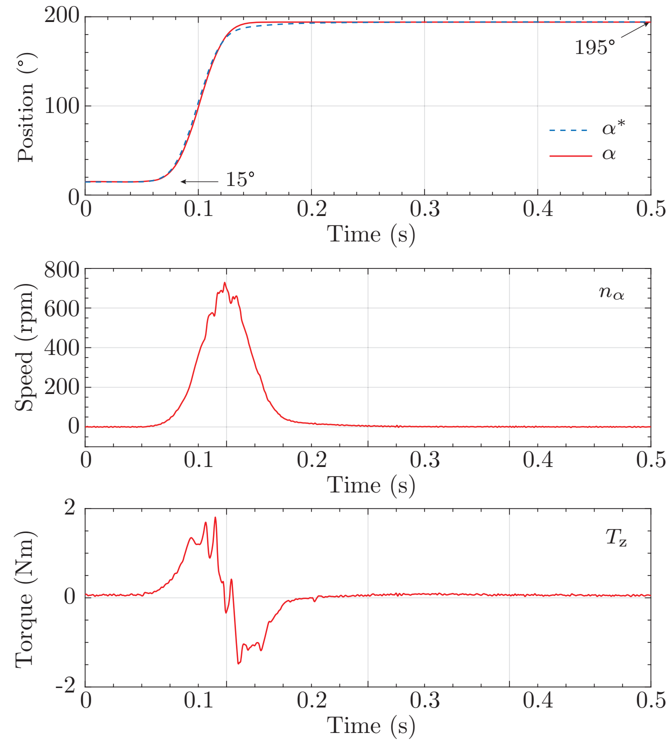

Fig. 16: Rotary angle sigmoid reference step response of the PID controller based rotary position control. The angular step is 180° and the maximum speed is around 700 rpm. The measurement is conducted with the mover being supported by magnetic bearings.

A. Torque/Force Constant Measurement

In order to verify the FEM models used for the optimization of the SBDS LiRA, flux linkages ($\hat{\Psi}_{\mathrm{rot}}$ and $\hat{\Psi}_{\mathrm{lin}}$) and torque/force constants (K_{T} and K_{L}) are measured. The measured flux linkage for the rotary actuator is estimated in a first step from the voltage constant measurement (cf. **Fig. 15(a)**), where the voltage constant is equal to $K_{\mathrm{V,rot}} = (N_{\mathrm{p,rot}}/2) \cdot \hat{\Psi}_{\mathrm{rot}}$. Therefore, the measured flux linkage of the rotary stator is equal to $K_{\mathrm{V,rot}} \cdot (2/N_{\mathrm{p,rot}}) = 0.1657\,\mathrm{V/(rad/s)}/8 = 20.71\,\mathrm{mWb}$, as given in **Tab. V**. The larger relative error for the torque constant can be attributed to mechanical friction of the auxiliary bearings that are used during these initial measurements. Since for the linear stator the flux linkage measurement is estimated from the linear force constant as $\hat{\Psi}_{\mathrm{lin}} = K_{\mathrm{L}} \cdot \tau_{\mathrm{pp}}/(3\pi)$, cf. [21], the relative error has the same value. Finally, **Tab. V** shows that the FEM simulation results and measurements are in good agreement, which verifies the used models.

B. PID Controller of the Rotary and Linear Position

To verify the operation of the SBDS LiRA and its inverter power supply, rotary position control and linear position control are analyzed separately. The implemented position controls are employing PID-type controllers.

In **Fig. 16** a step response of the rotary angle α is shown (see **Fig. 1** for the angle notation). The reference α^* follows a sigmoid shaped function with the rise time of around $50\,\mathrm{ms}$. The rotational PID controller gains are equal to $K_{\mathrm{p,rot}} = 25\,\mathrm{N/rad}$, $K_{\mathrm{i,rot}} = 99\,\mathrm{N/rad\,s}$ and $K_{\mathrm{d,rot}} = 0.8\,\mathrm{N\,s/rad}$, where the proportional gain is chosen such that a stable and highly dynamic control is achieved, which resulted in good reference tracking (cf. **Fig. 16**). The maximum occurring speed n_α is around $700\,\mathrm{rpm}$.

In **Fig. 17** a step response of the linear position z is depicted, where the reference z^* shows a sigmoid shape with a rise time of around $150\,\mathrm{ms}$. Again, a PID controller is tuned for high bandwidth, which results in the following gain values: $K_{\mathrm{p,lin}} = 125\,\mathrm{N/m}$, $K_{\mathrm{i,lin}} = 5862\,\mathrm{N/m\,s}$ and $K_{\mathrm{d,lin}} = 1\,\mathrm{N\,s/m}$. The maximum occurring linear speed is around $0.1\,\mathrm{m/s}$. The peculiar time behavior of the linear force results from the cogging forces, which show peak values of $\pm 30\,\mathrm{N}$.

The results shown in **Fig. 16** and **Fig. 17** verify the SBDS LiRA rotary and linear operation. In future work, a simultaneous rotary-linear operation will be tested.

VI. Conclusions

In this paper a design procedure for a selfbearing double-stator linear-rotary actuator (SBDS LiRA) is shown. The axial heat flow of the inner stator of the actuator is enhanced with an inserted copper pipe. A geometry optimization is performed which uses 2D FEM models coupled with an analytic thermal model. From the axial force $\vec{F}_{\mathrm{z}}$ vs. axial torque $\vec{T}_{\mathrm{z}}$ Pareto plots a design candidate is chosen and a hardware prototype

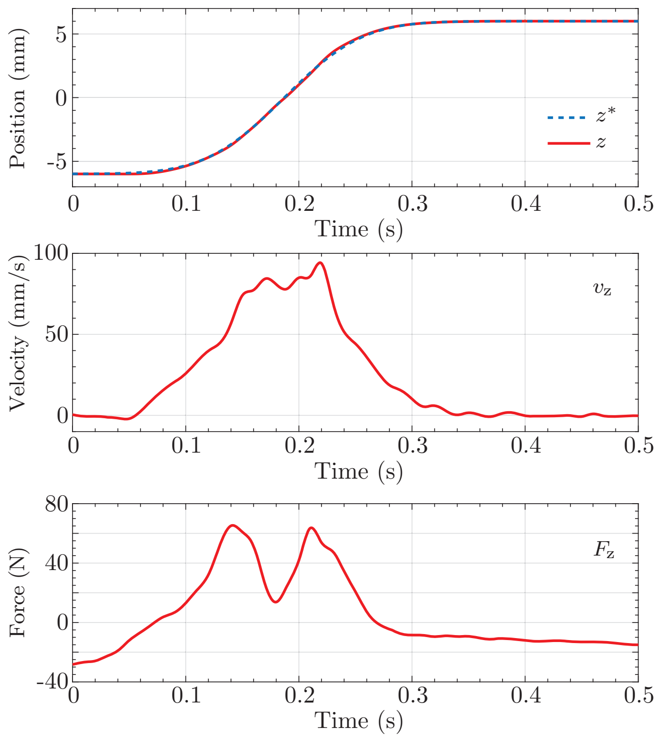

Fig. 17: Linear position sigmoid reference step response of the PID-based linear position control. The linear position stroke is $12\,\mathrm{mm}$ and the maximum linear speed is $0.1\,\mathrm{m/s}$. The linear force (F_z) has non zero steady-state value due to cogging force compensation. The measurement is conducted with the mover being supported by mechanical auxiliary linear bearings.

is assembled. To supply the SBDS LiRA, an 18-phase inverter supply is designed and a hardware prototype is built. Initial measurement results verify the used FEM models where the simulated and the measured SBDS LiRA torque constants differ by $8.7\,\%$. Measurement results of rotary and linear position step responses verify the SBDS LiRA rotary and linear stator operation.

Future work focuses on the simultaneous operation of the SBDS LiRA rotary and linear stators with full magnetic levitation. Furthermore, a detailed verification of the thermal properties and the maximum torque and force generation will be carried out.

References

[1] A. Turner, K. Ramsay, R. Clark, and D. Howe, "Direct-Drive Rotary-Linear Electromechanical Actuation System for Control of Gearshifts in Automated Transmissions," in *Proc. of IEEE Vehicle Power and Propulsion Conference*, Arlington, TX, USA, 2007.

[2] T. Overboom, J. Jansen, E. Lomonova, and F. Tacken, "Design and Optimization of a Rotary Actuator for a Two-Degree-of-Freedom $z-\varphi$ Module," *IEEE Transactions on Industry Applications*, vol. 46, no. 6, pp. 2401–2409, 2010.

[3] A. Mousavi, A. Akbarzadeh, M. Shariatee, and S. Alimardani, "Design and Construction of a Linear-Rotary Joint for Robotics Applications," in *Proc. of IEEE RSI International Conference on Robotics and Mechatronics (ICROM)*, Tehran, Iran, 2015, pp. 229–233.

[4] K. Meessen, J. Paulides, and E. Lomonova, "Analysis and Design Considerations of a 2-DoF Rotary-Linear Actuator," in *Proc. of IEEE International Electric Machines and Drives Conference (IEMDC)*, Niagara Falls, ON, Canada, 2011.

[5] S. Mirić, D. Bortis, and J. W. Kolar, "Design and Comparison of Permanent Magnet Self-Bearing Linear-Rotary Actuators," in *Proc. of 12th IEEE International Symposium on Linear Drives for Industry Applications (LDIA)*, Neuchatel, Switzerland, 2019.

[6] L. Xu, M. Lin, X. Fu, and N. Li, "Design and Analysis of a Double-Stator Linear-Rotary Permanent-Magnet Motor," *IEEE Transactions on Applied Superconductivity*, vol. 26, no. 4, pp. 1–4, 2016.

[7] H. Bleuler, M. Cole, P. Keogh, R. Larsonneur, E. Maslen, Y. Okada, G. Schweitzer, A. Traxler *et al.*, *Magnetic Bearings: Theory, Design, and Application to Rotating Machinery*. Springer Science & Business Media, 2009.

[8] Tolomatic, Excellence in Motion, Top 5 Best Practices for Designing Electric Actuators into Food Processing Equipment, https://www.tolomatic.com/info-center/resource-details/resourceid/1334 Accessed: 03/04/2021.

[9] Fischer Elektronik, Heatsink ICK S R 98 × 50, https://www.fischerelektronik.de Accessed: 03/04/2021.

[10] S. Mirić, A. Tüysüz, and J. W. Kolar, "Comparative Evaluation of Linear-Rotary Actuator Topologies for Highly Dynamic Applications," in *Proc. of IEEE International Electric Machines and Drives Conference (IEMDC)*, Miami, FL, USA, 2017.

[11] N. Simpson, R. Wrobel, and P. H. Mellor, "Estimation of Equivalent Thermal Parameters of Impregnated Electrical Windings," *IEEE Transactions on Industry Applications*, vol. 49, no. 6, pp. 2505–2515, 2013.

[12] Heiniger, Motor Cable TT-flex Eca PVC C 25 × 1.0 JZ 500 V, https://www.heiniger-ag.ch/de_CH/tt-flex-eca-pvc-c-25x1-00-jz-num-gr/g/888852253/98131 Accessed: 03/04/2021.

[13] Heiniger, Data Cable PVC C 25 × 2 × 0.14 DIN47100 30 V UL Style 2560, https://www.heiniger-ag.ch/de_CH/datenkabel-pvc-c-25x2x0-14-din47100-gr/g/999990252/98133# Accessed: 03/04/2021.

[14] R. W. Erickson, "Optimal Single Resistors Damping of Input Filters," in *Proc. of IEEE Applied Power Electronics Conference and Exposition (APEC)*, Dallas, TX, USA, 1999.

[15] M. Mauerer, A. Tüysüz, and J. W. Kolar, "Distortion Analysis of Low-THD/High-Bandwidth GaN/SiC Class-D Amplifier Power Stages," in *Proc. of IEEE Energy Conversion Congress and Exposition (ECCE)*, Montreal, QC, Canada, 2015.

[16] S. Mirić, P. Küttel, A. Tüysüz, and J. W. Kolar, "Design and Experimental Analysis of a New Magnetically Levitated Tubular Linear Actuator," *IEEE Transactions on Industrial Electronics*, vol. 66, no. 6, pp. 4816–4825, 2018.

[17] Infineon, *IGLD60R070D1 - 600V CoolGaN Enhancement Mode Power Transistor*, 2016.

[18] MAGTROL, *TM Series, In-Line Torque Transducers, Model 306, Nominal Rated Torque 5 Nm*, 2020.

[19] TE Connectivity Measurement Specialties, *FX1901 Compression Load Cell Datasheet*, 2017.

[20] OCTOGON Messtechnik, Tension/Compression - Beam Load Cell 200 N - FZA-200, https://www.octogon.org/en/product/force-weighing/tension-compression-beam-load-cell Accessed: 03/04/2021.

[21] S. Mirić, R. Giuffrida, D. Bortis, and J. W. Kolar, "Enhanced Complex Space Vector Modeling and Control System Design of Multiphase Magnetically Levitated Rotary-Linear Machines," *IEEE Journal of Emerging and Selected Topics in Power Electronics*, vol. 8, no. 2, pp. 1833–1849, 2019.